

# Generation of photon pairs through spontaneous four-wave mixing in thin nonlinear layers

CHANGJIN SON,<sup>1,2,\*</sup> SAMUEL PEANA,<sup>3</sup> OWEN MATTHIESSEN,<sup>3</sup>  
ARTEM KRYVOBOK,<sup>3</sup> ALEXANDER SENICHEV,<sup>3</sup> ALEXANDRA  
BOLTASSEVA,<sup>3</sup> VLADIMIR M. SHALAEV,<sup>3</sup> AND MARIA CHEKHOVA<sup>1,2</sup>

<sup>1</sup>Max Planck Institute for the Science of Light, 91058 Erlangen, Germany

<sup>2</sup>Friedrich-Alexander Universität Erlangen-Nürnberg, 91058 Erlangen, Germany

<sup>3</sup>School of Electrical & Computer Engineering, Birck Nanotechnology Center, Purdue University, 1205 West State Street, West Lafayette, Indiana 47907, USA

\*changjin.son@mpl.mpg.de

**Abstract:** Pairs of entangled photons are a key resource for photonic quantum technologies. The demand for integrability and multi-functionality suggests ‘flat’ platforms, such as ultrathin layers and metasurfaces, as sources of photon pairs. Despite the success in the demonstration of spontaneous parametric-down-conversion (SPDC) from such ‘flat’ sources, there are almost no works on spontaneous four-wave mixing (SFWM) – an alternative process to generate photon pairs. Meanwhile, SFWM can be implemented in any nanostructures, including isotropic and centrosymmetric ones, which are easier to fabricate than crystalline structures needed for SPDC. Here, we investigate photon pair generation through SFWM in subwavelength layers of amorphous silicon nitride (SiN) and study the effect of nitrogen content on the rate of pair emission. By observing two-photon interference between SFWM from the SiN layers and from the fused silica substrate, we find the third-order susceptibilities of layers with different nitrogen content. Finally, we demonstrate SFWM in lithium niobate, which is a second-order nonlinear material and where the direct SFWM can coexist with a cascaded process. Our results open a path for the implementation of SFWM in resonant ‘flat’ structures, such as metasurfaces.

## 1. Introduction

Pairs of entangled photons are of great importance for quantum technologies, including quantum communication, computation, and sensing. The usually employed means to generate such pairs are spontaneous parametric down-conversion (SPDC) and spontaneous four-wave mixing (SFWM), utilizing nonlinear susceptibilities of the second ( $\chi^{(2)}$ ) and third ( $\chi^{(3)}$ ) order, respectively. The need for more compact sources of photon pairs led to the implementation of SPDC on ‘flat’ platforms, such as ultrathin nonlinear layers [1], including those which are only few-atomic layers thick [2], nanoantennas [3], and resonant metasurfaces [4]. Importantly, the relaxed phase-matching condition in such sources [5] simplifies quantum state engineering. Such sources can be made of materials with very high nonlinearity [2, 6], provide tunable polarization [7–10] or spatial [11] entanglement, and enable several entanglement links [12] or directions of emission [13, 14] simultaneously. The pairs generated in thin layers feature very broad spectra in both angle and frequency as well as large degrees of continuous-variable entanglement [5]. Resonances in nonlinear metasurfaces enhance the rate of pair emission by several orders of magnitude [4, 9, 12], in the vicinity of resonance wavelengths.

All of the works mentioned above employ SPDC for the generation of photon pairs. Meanwhile, there are almost no experiments where entangled photons are obtained through SFWM in nanoscale sources, although this third-order process is widely used to obtain entangled photons from fibers [15], waveguides [16], and microresonators [17, 18]. Despite theoretical studies [19, 20], and experiments with seeded FWM [21–24], to the best of our knowledge, there is only a single paper on SFWM on a ‘flat’ platform, namely a 100 nm-thick layer of carbon nanotubes [25]. However, the relatively high absorbance of this material at telecom wavelengths [26, 27] makes it

difficult for applications.

Here, we demonstrate SFWM in sub-wavelength layers of silicon nitride (SiN) with various nitrogen concentrations. An increase in the N concentration reduces  $\chi^{(3)}$  [28–30] and thus the rate of photon pair emission, but at the same time it suppresses photoluminescence (PL), which is detrimental for nanoscale sources of photon pairs [31], and increases the damage threshold.

In SFWM, two pump photons at frequency  $\omega_p$  convert into a pair of photons at frequencies  $\omega_s$  (signal) and  $\omega_i$  (idler), so that the energy is conserved,  $\omega_s + \omega_i = 2\omega_p$ . The phase matching condition for the wavevectors  $k_{s,i,p}$  of the signal, idler, and pump photons,  $k_s + k_i = 2k_p$ , is satisfied automatically for a broad range of frequencies as long as the sample is thin enough or the dispersion is weak enough. In our experiment, the former is valid for the samples and the latter, for the fused silica substrate. This leads to the two-photon interference between the pairs generated from the sample and from the substrate. From this interference, we infer the contribution of the SiN layers into SFWM and eventually their  $\chi^{(3)}$  values.

Finally, we generate photon pairs in a second-order nonlinear material, namely lithium niobate (LN). In this case, SFWM competes with the cascaded  $\chi^{(2)}$  process, where photon pairs are generated via SPDC from the frequency-doubled pump radiation. However, as we show below, for the chosen thickness of the sample the  $\chi^{(2)}$  process is suppressed.

## 2. SFWM in subwavelength SiN layers

We fabricated samples with different N concentrations using high-density plasma chemical vapor deposition (HDPCVD, see the Supplemental Document). We studied SFWM in four samples with different thicknesses  $l$  and ratios  $x = N_2/SiH_4$  of the precursors (Table 1), all coated on  $500 \mu\text{m}$  fused silica substrates.

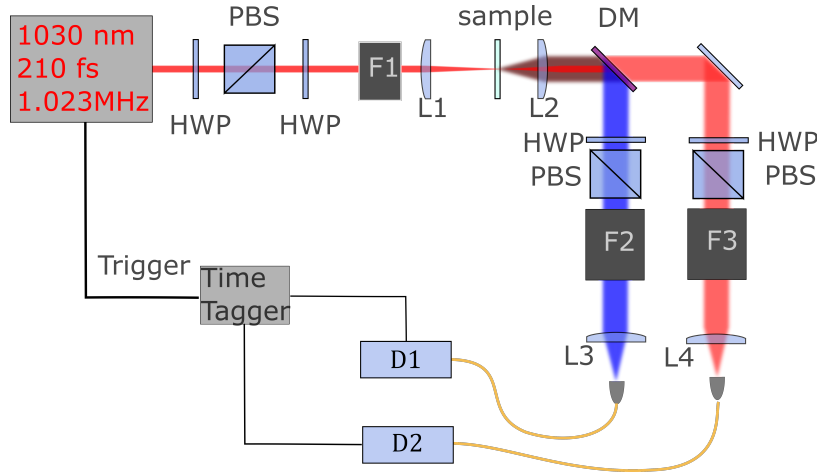


Fig. 1. Experimental setup. The pump is focused on the sample by lens L1. Signal and idler photons are collimated by lens L2, separated by dichroic mirror DM, coupled into multimode fibers by lenses L3, L4, and registered by detectors D1, D2, respectively. Their polarization is analyzed by a set of HWP and PBS in each arm. Filter sets (F1, F2, and F3) eliminate unwanted wavelengths. Photon detection events from D1, D2 are registered by a time tagger triggered by pulses from the laser.

As a pump (Fig.1) we use 210 fs pulses at wavelength 1030 nm and repetition rate 1.023 MHz. Its power and polarization can be varied using two half-wave plates (HWP) and a polarizing beam splitter (PBS). After cleaning the pump with filter F1, we focus it into a  $100 \mu\text{m}$  spot on the sample by lens L1 ( $f=100 \text{ mm}$ ). The generated photons are collimated by lens L2 ( $NA=0.5$ )

and spectrally separated by a long-pass dichroic mirror with the cut-on wavelength 950 nm. The SFWM spectrum is expected to extend from 650 nm to above 2  $\mu\text{m}$  but we set narrow detection bands to reduce the PL. Signal (visible) photons are filtered to 10 nm around 770 nm (F2) and idler (IR) photons, to 50 nm at 1550 nm (F3). Signal and idler photons are coupled by lenses L3 ( $f=30$  mm) and L4 ( $f=50$  mm) into 100  $\mu\text{m}$  multimode fibers and sent to single-photon detectors D1 (Perkin&Elmer, SPCM-AQRH-16-FC) and D2 (IDQ, ID220), respectively. The detection events are registered by the time tagger, triggered by pulses from the laser. This considerably reduces the effect of PL [31].

Table 1 summarizes the properties of our samples: N concentration  $x$ , thickness  $l$ , the third-order susceptibility evaluated from the third-harmonic generation (THG), see Supplementary Document, and the rates of PL per unit thickness. We see that the  $\chi^{(3)}$  continuously reduces with the increase of the nitrogen concentration, which is expected because nitrogen broadens the band gap and therefore brings the excitation further from the resonance. The level of PL also decreases; for instance, for sample D it is twice as low as for sample A, both at 1550 nm and at 770 nm (see the Supplemental Document for more detail).

Fig. 2 shows the results of measurements on sample C, all gated with electronic pulses from the laser. Still, single-photon counts (a) mostly come from the PL. For the IR channel (red), this is clear from the power dependence, which is linear while the rate of photon emission through SFWM should depend quadratically on the pump power. The rate of photons in the visible channel (blue) indeed has a quadratic dependence on the pump power. However, this emission is almost unpolarized (Fig. 2 b), while SFWM in an isotropic material such as SiN should be polarized similarly to the pump. The visible photons are then mostly emitted through two-photon pumped PL, which explains the quadratic dependence on their rate on the pump power. The IR PL is partially polarized because of the small (0.5 eV) frequency shift from the pump [32] (see the Supplemental Document for more detail). Fig. 2 (c) shows the mean number of coincidences per pulse measured versus the pump power. The dependence is quadratic at low power (red solid line) but becomes cubic (green dashed line) at stronger pumping because of the accidental coincidences resulting from the PL, which scales quadratically in the visible and linearly in the IR channel.

Finally, Fig. 2 (d) shows the second-order correlation function  $g^{(2)}(0) = \frac{\langle :N^2: \rangle}{\langle N \rangle^2}$ , measured as  $g^{(2)} \equiv \frac{\langle N_c \rangle}{\langle N_1 \rangle \langle N_2 \rangle}$  [33], where  $\langle N_{c,1,2} \rangle$  are the mean numbers of coincidences and counts in channels 1, 2 per pulse, respectively. The experimental points are well fitted by  $g^{(2)} = 1 + 1/(aP)$ , where  $a$  is a constant and  $P$  is the pump power, because of the linear dependence of the signal in the IR channel on the pump. The dependence of  $g^{(2)}$  on the pump power and its value exceeding 2 confirm the generation of photon pairs. Other samples also show high  $g^{(2)}$  values, see Fig. 3 (a). The maximal values of the second-order correlation function were measured at different

Sample	$x$	$l$ (nm)	$n_p$	$n_{IR}$	$n_{VIS}$	$\chi_{THG}^{(3)}$ ( $\text{m}^2/\text{V}^2$ )
A	0.18	811	2.93	2.87	3.04	$2.3 \times 10^{-18}$
B	0.37	500	2.63	2.58	2.71	$1.5 \times 10^{-18}$
C	0.56	679	2.33	2.31	2.39	$2.1 \times 10^{-19}$
D	0.75	477	2.18	2.17	2.21	$6.8 \times 10^{-20}$

Table 1. SiN samples used in the experiment, with various N concentrations  $x$ , thicknesses  $l$ , refractive indices at the pump, idler (IR) and signal (visible) wavelengths (1030 nm, 1550 nm, and 770 nm, respectively), and  $\chi^{(3)}$  measured from THG.

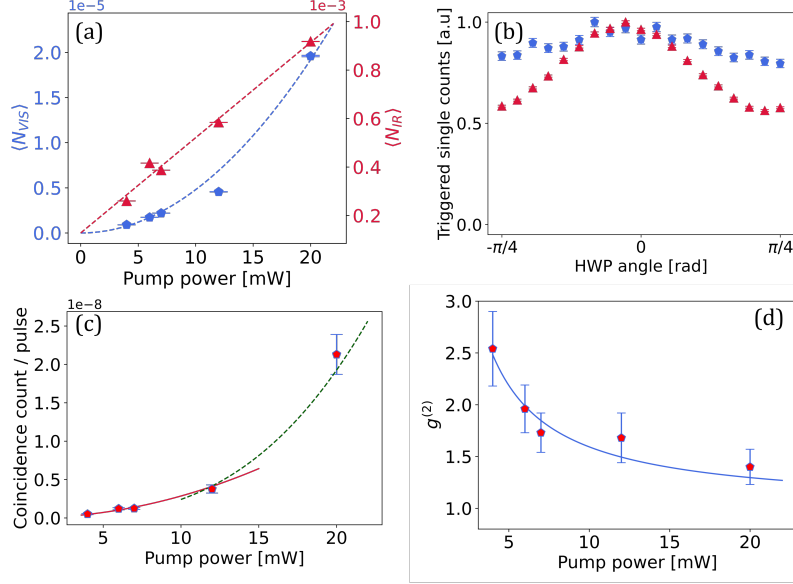


Fig. 2. SFWM in sample C. (a) Mean photon numbers per pulse at 770 (blue) and 1550 (red) nm vs the pump power, with linear and quadratic fits, respectively. (b) Polarization dependence of the mean photon numbers per pulse at 770 nm (blue) and 1550 nm (red).  $0^\circ$  corresponds to the pump polarization. (c) Mean numbers of coincidences per pulse vs the pump power, with the quadratic (solid) and cubic (dashed) fits. (d) The second-order correlation function vs the pump power.

pump powers, namely 4, 6, 4, and 16 mW for samples A, B, C, D, respectively, as samples with different  $x$  have different damage thresholds.

### 3. Two-photon interference

In Fig. 3 (b), we plot the SFWM rates for all samples as functions of the pump power circulating inside the layers (which is different from the incident power due to etalon effect). The mean numbers of coincidences per pulse are plotted after subtracting the numbers of accidental coincidences. The latter are estimated as the products of D1 and D2 photocount numbers per pulse. The scaling, as expected, is quadratic in the pump power for all samples.

The figure also includes the results obtained for the bare fused silica (FS) substrate, which demonstrate similar rates of SFWM. This is unsurprising: although  $\chi^{(3)}$  for SiN is three orders of magnitude higher than that of FS ( $3 \cdot 10^{-22} \text{m}^2/\text{V}^2$  [34]), the SiN layers are three orders of magnitude thinner than the substrate (Table 1). Note that the SFWM coherence length in FS is  $486 \mu\text{m}$  and hence almost all the substrate contributes to SFWM.

What can be surprising is that the rate of SFWM from sample B, coated on the substrate, is significantly lower than from the substrate alone. An explanation comes if we account for the quantum interference between the probability amplitudes of a photon pair emission from the SiN layer and the substrate. Following the approach of Ref. [35], we obtain that the two-photon state generated in the ‘layer-substrate’ structure is

$$|\Psi\rangle \propto [A_l + e^{i(\Delta k_l l + \Delta k_{sub} L)/2} A_{sub}] |1\rangle_i |1\rangle_s, \quad (1)$$

where  $A_{l,sub}$  are the amplitudes of pair emission in the layer and the substrate, respectively,  $\Delta k_{l,sub}$  the corresponding wavevector mismatches,  $l$  and  $L$  the lengths of the layer and the

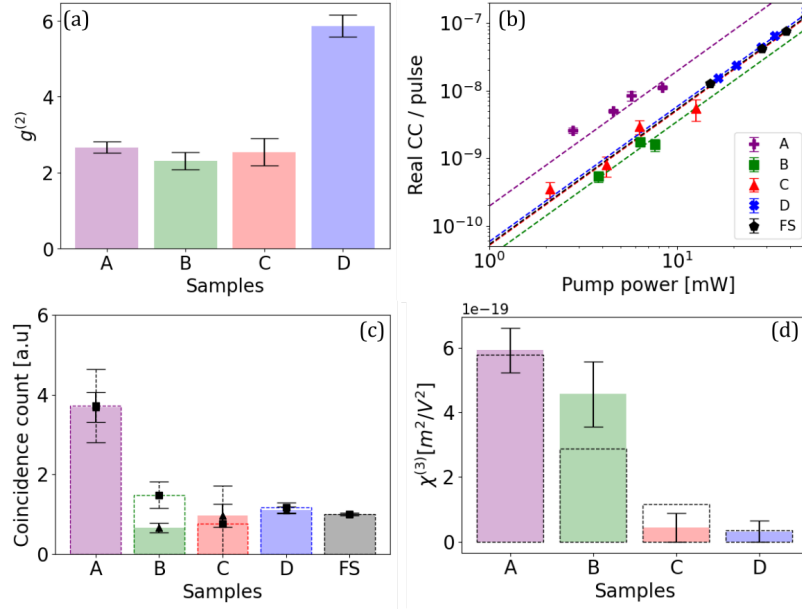


Fig. 3. (a) Maximal  $g^{(2)}$  values obtained for samples A, B, C, and D. (b) Numbers of real coincidences per pulse vs the pump power for samples A-D and the FS, with quadratic fits. (c) Coincidence count rates under the same pump power inside the layers. The solid and dashed bars are for the detection band pairs, respectively, {1550 nm, 770 nm} and {1450 nm, 800 nm}. (d) The  $\chi^{(3)}$  values measured (solid bars) and estimated from Miller's rule (dashed bars).

substrate, and  $|1\rangle_{s,i}$  signal and idler single-photon states. The rate of SFWM pairs is then

$$R \propto A_l^2 + A_{sub}^2 + 2A_l A_{sub} \cos(\Delta\phi), \quad (2)$$

where the interference phase  $\Delta\phi = (\Delta k_s L + \Delta k_l l)/2$ . Meanwhile, for the substrate alone, the rate is  $R_{sub} \propto A_{sub}^2$ .

Calculating the phase mismatch  $\Delta k = k_s + k_i - 2k_p$ , we find that  $\Delta k_{sub} L/2 = 0.51\pi$ , while  $\Delta k_l l/2$  take values between  $0.01\pi$  and  $0.08\pi$ . Overall, the interference phase is between  $0.52\pi$  and  $0.60\pi$ , which leads to destructive interference for all samples. This explains why sample B on a substrate yields fewer pairs than the substrate alone.

The rates of real coincidences under the same pump power (circulating in the case of the layers) are plotted in Fig. 3 (c) as solid bars. We now change the interference phase by choosing other wavelengths of the signal and idler photons: 800 nm and 1450 nm, respectively. Because of the slow dispersion, the only significant result of passing to these wavelengths is that the phase  $\Delta k_{sub} L/2$  becomes  $0.39\pi$ , which turns destructive interference into constructive one. The corresponding real coincidence rates (Fig. 3 (c), dashed bars) are indeed higher than in the previous case, except for sample C where the uncertainty is too large.

Using Eq. (2) for constructive and destructive interference, we find the ratio  $A_l/A_{sub}$  for each SiN layer. Meanwhile [36],

$$A_l \propto \frac{\chi_l^{(3)}}{n_p} \cdot P_c \cdot l \cdot \text{sinc}(\Delta k_l l/2) \cdot \sqrt{T_s \cdot T_i}, \quad (3)$$

where  $n_p$  is the pump refractive index,  $\chi_l^{(3)}$  the third-order susceptibility for SFWM,  $P_c$  the pump power inside the layer, and  $T_{s,i}$  the transmission coefficients for the output photons (see the

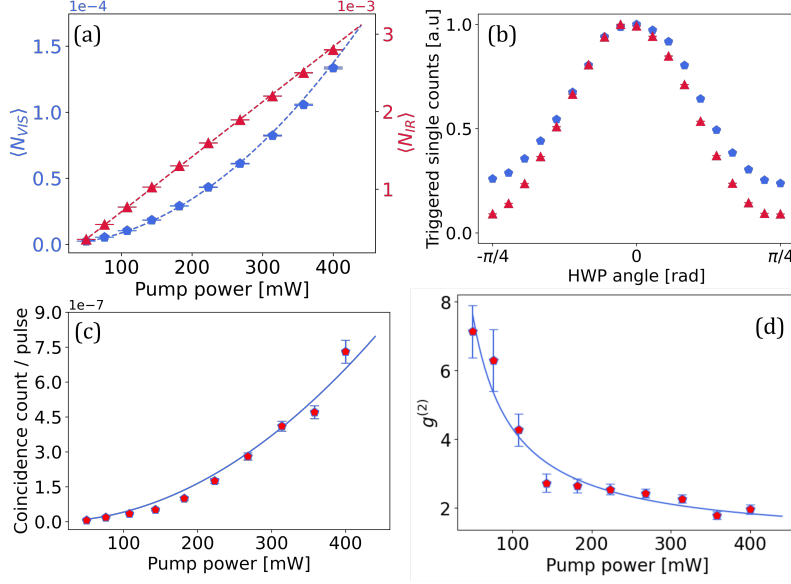


Fig. 4. SFWM in the LN layer. (a) Numbers per pulse of visible (blue) and IR (red) photons vs the pump power, and their fits. (b) Polarization dependence of the number per pulse of visible (blue) and IR (red) photons. The angle  $0^\circ$  corresponds to the pump polarization. (c) Number of coincidences per pulse vs the pump power, with a quadratic fit. (d) Second-order correlation function vs the pump power and its fit.

Supplementary document for details). A similar expression is valid for  $A_{\text{sub}}$ , with  $P_c$  replaced by the pump power transmitted by the layer.

Finally, from Eq. (3), knowing  $\chi^{(3)}$  for FS, we obtain its values for the samples (Fig. 3 (d)). For samples C and D, the low contribution of the layers compared to the one of the substrate leads to large uncertainty; as a result, only the upper limit for  $\chi^{(3)}$  is available. The results agree reasonably well with the ones predicted by Miller's rule (dashed bars).

#### 4. SFWM in lithium niobate

We also studied SFWM in a  $\chi^{(2)}$  material, where SFWM can occur simultaneously with a cascaded process. The sample is a  $10 \mu\text{m}$  thick layer of X-cut LN on a fused silica substrate. The setup is the same as in Fig. 1, with the pump polarization set parallel to the optic axis of LN.

Fig. 4 (a) presents the rates of photon detection in both channels vs the mean pump power, which now can be very high because LN is highly transparent at 1030 nm. Similarly to the case of SiN, the number of visible photons scales quadratically with the pump power, while the number of IR photons scales linearly. However, the origin of this behavior is different now. Because LN is transparent at 1030 nm, the PL is much weaker than for SiN. This is confirmed by the strong polarization dependence (Fig. 4 (b)) of the visible and especially IR photons rates. The visible photons then come mostly from SFWM, which explains the quadratic dependence of their emission rate on the pump power (Fig. 4 (a), blue).

To explain the linear dependence of the IR photons rate on the pump power (Fig. 4 (a), red), we now recall that the LN layer pumped at 1030 nm should generate pairs of IR and mid-infrared (MIR) photons, for instance, 1550 nm and 3080 nm, via SPDC supported by the  $\chi_{\text{zzz}}^{(2)}$  component of the second-order susceptibility tensor. The coherence length for this process is  $15 \mu\text{m}$ ; therefore, the whole layer contributes. The MIR photons cannot be detected, but their

'partners' at 1550 nm constitute most of the counts in the IR channel. Their rate should then scale linearly in the pump power, which is typical for SPDC, and follow the polarization dependence of Fig. 4 (b).

Photon pairs at 770 nm and 1550 nm are then due to SFWM. Accordingly, the coincidence rate scales quadratically with the pump power (Fig. 4 (c)). It is also considerably higher than for SiN, and leads to higher  $g^{(2)}$  (Fig. 4 (d)) because of low PL.

Cascaded SFWM can run via the second harmonic generation (SHG) from 1030 nm followed by SPDC [37, 38]. The coherence lengths for these two processes are, respectively, 3.1  $\mu\text{m}$  and 3.2  $\mu\text{m}$ . To identify the contribution of the cascaded process, we additionally make two measurements: of the second harmonic at 515 nm generated by the sample and of SPDC pumped at 515 nm from an external source. From these measurements, we estimate the contribution of the cascaded process to the coincidence rate (see the Supplementary Document for details) to be only 5%.

## 5. Conclusion

We have generated photon pairs through SFWM in sub-wavelength SiN layers. Although most of the detected photons are from the PL, we could identify photon pairs through the  $g^{(2)}$  measurement. As the nitrogen concentration increases, the  $\chi^{(3)}$  reduces, but so does the PL.

Because SFWM has a large coherence length, it inevitably occurs in the substrate as well. We show that it can lead to an interference between pair generation in the layer and in the substrate. This fact, not considered so far, can strongly affect experiments on entangled photon generation via SFWM in 'flat' sources. In particular, destructive interference can be turned into constructive interference by changing the thicknesses of the layer and the substrate or by passing to different wavelengths.

We also implemented SFWM in a  $\chi^{(2)}$  material (LN), where SFWM can run through both cascaded and direct routes. Here, the contribution of the cascaded process is negligible because the thickness of the layer exceeds three times the coherence length of the cascaded process while being much shorter than that of direct SFWM. As a result, we could utilize the whole thickness for direct SFWM. This effect will be more obvious if the LN thickness is an even multiple of the SHG coherence length.

We believe this study opens the possibility of using thin dielectric platforms with third-order nonlinearity for generating entangled photons. The pair generation rates in our experiments are very low, but they can be improved by structuring the material and using geometric resonances.

## References

1. T. Santiago-Cruz, V. Sultanov, H. Zhang, *et al.*, "Entangled photons from subwavelength nonlinear films," *Opt. Lett.* **46**, 653–656 (2021).
2. Q. Guo, X.-Z. Qi, L. Zhang, *et al.*, "Ultrathin quantum light source with van der waals nbocl2 crystal," *Nature* **613**, 53–59 (2023).
3. G. Marino, A. S. Solntsev, L. Xu, *et al.*, "Spontaneous photon-pair generation from a dielectric nanoantenna," *Optica* **6**, 1416–1422 (2019).
4. T. Santiago-Cruz, A. Fedotova, V. Sultanov, *et al.*, "Photon pairs from resonant metasurfaces," *Nano letters* **21**, 4423–4429 (2021).
5. C. Okoth, A. Cavanna, T. Santiago-Cruz, and M. V. Chekhova, "Microscale generation of entangled photons without momentum conservation," *Phys. Rev. Lett.* **123**, 263602 (2019).
6. L. Kallioniemi, X. Lyu, R. He, *et al.*, "Van der waals engineering for quantum-entangled photon generation," *Nat. Photonics* pp. 1–7 (2024).
7. V. Sultanov, T. Santiago-Cruz, and M. V. Chekhova, "Flat-optics generation of broadband photon pairs with tunable polarization entanglement," *Opt. Lett.* **47**, 3872–3875 (2022).
8. J. Ma, J. Zhang, Y. Jiang, *et al.*, "Polarization engineering of entangled photons from a lithium niobate nonlinear metasurface," *Nano Lett.* **23**, 8091–8098 (2023).
9. J. Ma, T. Fan, T. Haggren, *et al.*, "Generation of tunable quantum entanglement via nonlinearity symmetry breaking in semiconductor metasurfaces," *arXiv preprint arXiv:2409.10845* (2024).

10. M. A. Weissflog, A. Fedotova, Y. Tang, *et al.*, “A tunable transition metal dichalcogenide entangled photon-pair source,” *Nat. Commun.* **15**, 7600 (2024).
11. J. Zhang, J. Ma, M. Parry, *et al.*, “Spatially entangled photon pairs from lithium niobate nonlocal metasurfaces,” *Sci. Adv.* **8**, eabq4240 (2022).
12. T. Santiago-Cruz, S. D. Gennaro, O. Mitrofanov, *et al.*, “Resonant metasurfaces for generating complex quantum states,” *Science* **377**, 991–995 (2022).
13. C. Son, V. Sultanov, T. Santiago-Cruz, *et al.*, “Photon pairs bi-directionally emitted from a resonant metasurface,” *Nanoscale* **15**, 2567–2572 (2023).
14. M. A. Weissflog, J. Ma, J. Zhang, *et al.*, “Directionally tunable co-and counterpropagating photon pairs from a nonlinear metasurface,” *Nanophotonics* **13**, 3563–3573 (2024).
15. J. E. Sharping, M. Fiorentino, A. Coker, *et al.*, “Four-wave mixing in microstructure fiber,” *Opt. Lett.* **26**, 1048–1050 (2001).
16. H. Fukuda, K. Yamada, T. Shoji, *et al.*, “Four-wave mixing in silicon wire waveguides,” *Opt. Express* **13**, 4629–4637 (2005).
17. T. Kippenberg, S. Spillane, and K. Vahala, “Kerr-nonlinearity optical parametric oscillation in an ultrahigh-q toroid microcavity,” *Phys. Rev. Lett.* **93**, 083904 (2004).
18. H. Wang, Q. Zeng, H. Ma, and Z. Yuan, “Progress on chip-based spontaneous four-wave mixing quantum light sources,” *Adv. Devices & Instrum.* **5**, 0032 (2024).
19. L. Xu, D. A. Smirnova, R. Camacho-Morales, *et al.*, “Enhanced four-wave mixing from multi-resonant silicon dimer-hole membrane metasurfaces,” *New J. Phys.* **24**, 035002 (2022).
20. C. Yuan, W. Zhang, and Y. Huang, “Spatiotemporally separable biphoton state generated by spontaneous four wave mixing in ultrathin nonlinear films,” *arXiv preprint arXiv:1903.10936* (2019).
21. M. P. Nielsen, X. Shi, P. Dichtl, *et al.*, “Giant nonlinear response at a plasmonic nanofocus drives efficient four-wave mixing,” *Science* **358**, 1179–1181 (2017).
22. J. Yang, P. Dichtl, J. Flórez, *et al.*, “Stimulated emission tomography analysis of plasmonic nanoantennas,” in *Active Photonic Platforms 2022*, vol. 12196 (SPIE, 2022), pp. 78–84.
23. L. Caspani, R. Kaipurath, M. Clerici, *et al.*, “Enhanced nonlinear refractive index in  $\epsilon$ -near-zero materials,” *Phys. Rev. Lett.* **116**, 233901 (2016).
24. E. G. Carnemolla, W. Jaffray, M. Clerici, *et al.*, “Visible photon generation via four-wave mixing in near-infrared near-zero-index thin films,” *Opt. Lett.* **46**, 5433–5436 (2021).
25. K. F. Lee, Y. Tian, H. Yang, *et al.*, “Photon-pair generation with a 100 nm thick carbon nanotube film,” *Adv. Mater.* **29**, 1605978 (2017).
26. T. Nishihara, A. Takakura, M. Shimasaki, *et al.*, “Empirical formulation of broadband complex refractive index spectra of single-chirality carbon nanotube assembly,” *Nanophotonics* **11**, 1011–1020 (2022).
27. B. Song, F. Liu, H. Wang, *et al.*, “Giant gate-tunability of complex refractive index in semiconducting carbon nanotubes,” *ACS Photonics* **7**, 2896–2905 (2020).
28. T. Ning, O. Hyvärinen, H. Pietarinen, *et al.*, “Third-harmonic uv generation in silicon nitride nanostructures,” *Opt. Express* **21**, 2012–2017 (2013).
29. D. Tan, K. Ooi, and D. Ng, “Nonlinear optics on silicon-rich nitride—a high nonlinear figure of merit cmos platform,” *Photonics Res.* **6**, B50–B66 (2018).
30. B. Ding, X. Yu, H. Lu, *et al.*, “Third-order optical nonlinearity in silicon nitride films prepared using magnetron sputtering and application for optical bistability,” *J. Appl. Phys.* **125** (2019).
31. V. Sultanov and M. Chekhova, “Temporally distilled high-dimensional biphotonic states from thin sources,” *ACS Photonics* **11**, 2–6 (2023).
32. J. Diener, Y. Shen, D. Kovalev, *et al.*, “Two-photon-excited photoluminescence from porous silicon,” *Phys. Rev. B* **58**, 12629 (1998).
33. O. A. Ivanova, T. S. Iskhakov, A. N. Penin, and M. V. Chekhova, “Multiphoton correlations in parametric down-conversion and their measurement in the pulsed regime,” *Quantum Electron.* **36**, 951 (2006).
34. R. W. Boyd, A. L. Gaeta, and E. Giese, “Nonlinear optics,” in *Springer Handbook of Atomic, Molecular, and Optical Physics*, (Springer, 2008), pp. 1097–1110.
35. D. Klyshko, “Ramsey interference in two-photon parametric scattering,” *JETP* **104**, 2676–2684 (1993).
36. L. Wang, C. Hong, and S. Friberg, “Generation of correlated photons via four-wave mixing in optical fibres,” *J. Opt. B: Quantum semiclassical optics* **3**, 346 (2001).
37. M.-s. Kim and C. S. Yoon, “Theoretical analysis of third-harmonic generation via direct third-order and cascaded second-order processes in cslib 6 o 10 crystals,” *Phys. Rev. A* **65**, 033831 (2002).
38. S. M. Saltiel, A. A. Sukhorukov, and Y. S. Kivshar, “Multistep parametric processes in nonlinear optics,” in *Progress in optics*, vol. 47 (Elsevier, 2005), pp. 1–73.